PDF calculations of turbulent lifted flames of H_2/N_2 fuel issuing into a vitiated co-flow

A R Masri[1,4]**, R Cao**[2]**, S B Pope**[2] **and G M Goldin**[3]

[1] School of Aerospace, Mechanical and Mechatronic Engineering, The University of Sydney, NSW 2006, Australia
[2] Mechanical and Aerospace Engineering, Cornell University, Ithaca, NY 14850, USA
[3] Fluent Inc, Lebanon, New Hampshire, USA

Abstract
This paper presents detailed calculations of the flow, mixing and composition fields of a simple jet of hydrogen–nitrogen mixture issuing into a vitiated co-flowing stream. The co-flow contains oxygen as well as combustion products and is sufficiently hot to provide an ignition source for a flame that stabilizes at some ten diameters downstream of the jet exit plane. This configuration forms a good model problem for studying lifted flames as well as issues of auto-ignition.

The calculations employ a composition probability density function (PDF) approach coupled to the commercial CFD package FLUENT. The *in situ* adaptive tabulation method is adopted to account for detailed chemical kinetics. A simple k–ε model is used for turbulence along with a low Reynolds number model for the walls. Calculations are optimized to obtain a numerically accurate solution and are repeated for two different H_2 mechanisms, each consisting of ten species. The flame is found to be largely controlled by chemical rather than mixing processes. The mechanisms used yield different lift-off heights and compositions that straddle the data. Ignition delays are found to be extremely sensitive to the chemical kinetic rates of some reactions in the mechanisms.

(Some figures in this article are in colour only in the electronic version)

1. Introduction

Despite the apparent simplicity of the flow, lifted flames continue to pose a challenge to modellers due to the outstanding difficulty in understanding the stabilization processes. There are many theories and hypotheses proposed for lifted flame stabilization [1, 2], all of which remain unproven due to the lack of reliable data. A comprehensive review of flame stabilization theories may be found in Pitts [3]. Until recently, only global measurements of lift-off heights were available and these were used to generate empirical correlations for lifted flames [4–9].

---

[4] Author to whom any correspondence should be addressed.

However, this scenario is gradually changing and detailed single point data as well as planar images of a range of scalars taken at the base of lifted flames have recently appeared in [10–13]. The difficulty, both experimentally and numerically, lies in the fact that the flame at the stabilization base is unstable and involves a significant degree of interaction between chemical and flow timescales. Spontaneously, the flame zone appears to reside where a balance between these interacting processes is reached [11]. Accounting for such interactions requires the use of detailed chemical kinetics as well as correct representation of the flow-field.

In a recent breakthrough in the computation of turbulent non-premixed combustion, Tang *et al* [14] and Lindstedt *et al* [15] have used the probability density function (PDF) approach with detailed chemical kinetics to compute extinction and re-ignition processes in pilot-stabilized diffusion flames. Although the approaches of the two groups differ in the use of mixing models, chemical kinetics and its implementation, they constitute the first direct and detailed computations of finite-rate chemistry effects in diffusion flames. Lindstedt and Louloudi [16] have recently extended the approach to piloted flames of methanol fuel while Liu *et al* [17] have performed successful computations of finite-rate chemistry effects in the more complex bluff-body stabilized flames of methane–hydrogen fuels. Conditional moment closure approaches [18–20] are gradually developing capabilities for computing finite-rate chemistry effects with the introduction of second order methods or second level of conditioning. However, large eddy simulations [21] remain largely constrained by huge computational requirements.

Another issue that is relevant to lifted flames as well as to engine combustion in general is the auto-ignition that occurs when reactive mixtures encounter hot pockets of air or combustion products. The chemical reactions that control auto-ignition may not necessarily be the same as those controlling steady combustion. In the flames considered here, the flames are largely controlled by chemical kinetics and hence the correct representation of the chemistry is critical. Numerical and theoretical studies of auto-ignition [22–28] have shown that mixtures do not necessarily ignite at stoichiometric mixture fraction but rather at mixture fractions where the fluid is most reactive yet the scalar dissipation rate is relatively low. Direct numerical simulations are proving to be an extremely useful tool in furthering current understanding of auto-ignition [24–28]. However, laboratory experiments investigating this phenomenon are rather scarce. Dally *et al* [29] have presented a detailed experimental study of a turbulent jet of H_2/CH_4 issuing into a stream of hot combustion products where the oxygen level is varied. Although this flow configuration is referred to as flameless or moderate and intense low oxygen dilution (MILD) combustion, it is closely related to auto-ignition.

This paper addresses both issues of auto-ignition and lifted flame stabilization. It presents calculations for turbulent jets of H_2/N_2 issuing in a wide co-flow of hot gas mixtures. The jet fluid mixes with co-flowing combustion products and heated air and subsequently auto-ignites, forming a lifted flame stabilized at about ten jet diameters downstream of the exit plane. This burner, developed by Cabra *et al* [30], has the advantage of representing both lift-off and auto-ignition in a rather simple and well-defined flow configuration. However, it should be noted that lifted flames issuing in vitiated co-flow are different from those stabilized in still air. The temperature and composition of the co-flow impose different conditions such that the controlling processes and the dynamics of flame stabilization are different from a regular lifted flame. Extensive composition data have been provided by Cabra [31] and these are used here for comparisons with the calculations.

2. The burner

Figure 1 shows a schematic of the burner and the computational domain used in the current calculations. The fuel jet, which has an inner diameter $D = 4.57$ mm and a wall thickness of

(a)   (b)
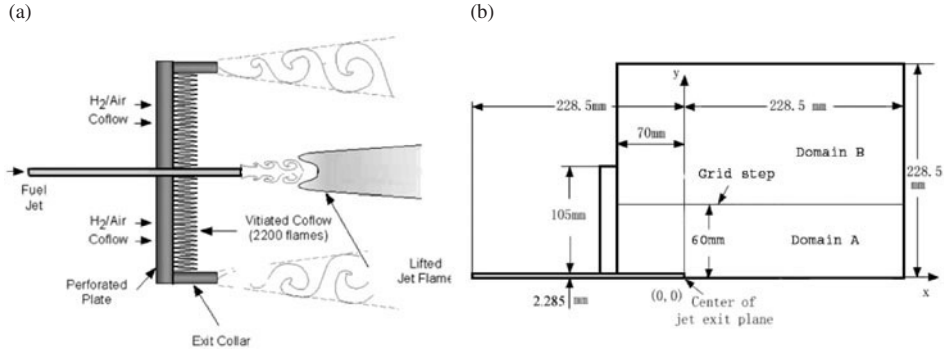
Figure 1. Schematic of (*a*) the burner and (*b*) the computational domain.

Table 1. Experimental conditions for the reacting and non-reacting jets.

	Non-reacting case		Reacting case	
	Jet	Pilot	Jet	Pilot
Velocity (m s^{-1})	170	4.4	107	3.5
ξ_s	—	—	0.47	—
Φ	—	0.31	—	0.25
T (K)	310	1190	305	1045
$X(O_2)$	0.21	0.135	0	0.1474
$X(N_2)$	0.79	0.741	0.75	0.7532
$X(H_2O)$	0	0.124	0	0.0989
$X(H_2)$	0	0	0.25	0
$X(OH)$	0	0	0	0.0005

0.89 mm, is located at the centre of a perforated disc that has a diameter of 210 mm. The disc has 2200 × 1.58 mm diameter holes that stabilize as many premixed flames, providing a hot co-flowing stream with a temperature and composition that are outlined in table 1. The overall blockage of the perforated plate is 87%. The central fuel jet extends by 70 mm downstream of the surface of the perforated plate so that the fuel mixture exits in a uniform composition for the co-flow. The entire burner assembly is shrouded with a water jacket for cooling and sits in stagnant air. The surrounding air does not affect the central jet for the axial locations discussed in this paper (which extend to about $x/D = 26$).

Two sets of measurements are available for this flow configuration, one for a non-reacting jet of air and the other for a lifted flame, both issuing in a vitiated co-flow. The burner was located in the wind tunnel at the Combustion Research Facility, Sandia National Laboratories, where detailed single point measurements of temperature and composition were made using the Raman–Rayleigh–LIF technique. The mass fractions of N$_2$, O$_2$, H$_2$O, OH and NO were measured and the data have been made available by Sreedhara and Lakshmisha [24]. Further details of the measurement technique, calibration and accuracy of the data may be found elsewhere [30]. Measurements of the flow-field are not yet available. Details of the conditions and characteristics of both cases are shown in table 1.

3. PDF computations

All computations presented here use the FLUENT package, which solves Reynolds averaged Navier–Stokes (RANS) equations for the mean conservation of mass, momentum and energy,

Table 2. Numerical conditions selected for computing the jet and flame in a vitiated co-flow.

Domain	Axisymmetric
Solver	Steady, segregated with implicit formulation
Turbulence model	Standard k–ε with
	$C_\mu = 0.09$, $C_{\varepsilon 1} = 1.44$, $C_{\varepsilon 2} = 1.92$, $\sigma_k = 1.0$, $\sigma_\varepsilon = 1.3$, $\sigma_\Phi = 0.7$
Mixing model	Modified Curl, $C_\phi = 2.0$ (for the base case)
Wall treatment	Low Reynolds number model
Discretization schemes	Presto for pressure
	PISO for pressure–velocity coupling
	Second order upwind for momentum and turbulent kinetic energy
Under relaxation factors	Pressure = 0.3, density = 1.0, body forces = 1, momentum = 0.7
Local time stepping	Courant number = 0.5

together with the k–ε turbulence model equations. A transport equation for the composition PDF is coupled and solved using a Lagrangian particle-based Monte Carlo method. In the flows considered here, the density computed from the thermochemical field has to be consistent with that computed from the flow-field as this constitutes the only link between the PDF and the RANS sections of the code. Although two mixing models may be used, interaction by exchange with the mean (IEM) and modified Curl (MC), only the MC model is used in this paper. A detailed chemical kinetic mechanism and a thermodynamic database are read in and the change in composition due to chemical reaction is then handled by the *in situ* adaptive tabulation (ISAT) method developed by Pope [32]. The use of ISAT is novel in this hybrid RANS–PDF approach. The numerical schemes used for both reacting and non-reacting calculations are detailed in table 2.

The non-reacting case is simulated as a two-stream problem where the different stream densities are caused by the different composition as well as temperature. The origin is taken at the centre of the jet exit plane. The computational domain is also shown in figure 1 and extends in the co-flowing stream from the face of the pilot plate down to 50 jet diameters downstream ($x = 228.5$ mm). Computations in the fuel line are initiated some 50 jet diameters upstream of the exit plane ($x = -228.5$ to $+228.5$ mm). The domain also extends radially out from the centreline to 50 jet diameters (from $y = 0$ to 228.5 mm).

For the reacting case, two chemical mechanisms are used for hydrogen. One mechanism is developed by Mueller *et al* [33] and involves ten species (H_2, H, O, O_2, OH, H_2O, HO_2, H_2O_2, Ar, N_2) and 21 reactions. The other is generated from the GRI-2.1 mechanism [34] for methane by stripping out all the carbon and NO containing species and reactions. This mechanism involves the same species as the Mueller *et al* [33] mechanism but with 28 reactions. These mechanisms are presented in full in the appendix and are referred henceforth as Mueller-H_2 and GRI21-H_2. It should be noted here that this is not meant to be a comparative study between hydrogen mechanisms but rather an exploration of auto-ignition issues in lifted flames issuing in a vitiated co-flow. Other detailed mechanisms of hydrogen [35–37] may also be used here and these may shed new light on the auto-ignition process. The objective, however, is to have only one optimal mechanism that may be used by modellers to represent the auto-ignition of hydrogen.

3.1. Boundary conditions

The boundary conditions used in the calculations are detailed in table 3. It should be noted here that for the non-reacting case, the detailed composition of the pilot is not accounted for and hence not detailed in table 3. Only one species is assumed to issue from the jet stream and another species of a different density is assumed to issue from the pilot stream. Detailed

Table 3. Boundary conditions for the non-reacting and reacting jets.

Stream	Condition	Non-reacting jet	Lifted flame
Fuel jet	Velocity (m s^{-1})	170	107
	Turbulent kinetic energy (m^2 s^{-2})	1.0	1.0
	Turbulence dissipation rate (m^2 s^{-3})	1.0	1.0
	Temperature (K)	310	305
	Y(H$_2$)	—	0.023 44
	Y(Ar)	—	0.01
	Density, ρ (kg m^{-3})	0.854	0.859
Pilot co-flow	Velocity (m s^{-1})	4.4	3.5
	Turbulent intensity (%)	5.0	5.0
	Turbulence length scale (mm)	1.0	1.0
	Temperature (K)	1190	1045
	Y(O$_2$)	—	0.170 92
	Y(OH)	—	0.000 31
	Y(H$_2$O)	—	0.064 56
	Density, ρ (kg m^{-3})	0.322	0.322
Jet wall	Wall with zero heat flux (adiabatic)		
Outer wall	Symmetry		
Outflow	Pressure outlet		

Table 4. Relevant information about the various meshes used in the calculations.

	X		Y		Mesh 1		Mesh 2		Mesh 3	
	From (mm)	To (mm)	From (mm)	To (mm)	Cells X	Cells Y	Cells X	Cells Y	Cells X	Cells Y
Fuel jet	−228.5	0	0	2.285	27	5	54	10	108	20
Pilot stream A	−70	0	2.285	60	11	31	22	62	44	124
Pilot stream B	−70	0	60	228.5	11	14	22	28	44	28
Main domain A	0	228.5	0	60	38	19	76	38	152	~76
Main domain B	0	228.5	60	228.5	38	31	76	62	152	~62
Total cells					2530		10 120		29 707	

conditions for the lifted flame case are detailed in table 3 in terms of species mass fractions, which are specified as boundary conditions.

4. Numerical issues

4.1. Grid and statistical convergence

The solution domain, shown in figure 1, is axisymmetric about the x-axis while y and r are used interchangeably to denote the radial coordinate. The solution domain is subdivided into five regions that are then meshed as described in table 4. The meshing is non-uniform, and in order to reduce the aspect ratio, some cells are made non-orthogonal. Mesh 2 is generated by dividing each cell in mesh 1 into four cells. In the third mesh, cells of mesh 2 extending radially up to $y = 60$ mm are divided by four while the remaining cells that are beyond $y = 60$ mm are not changed. The total number of cells in meshes 1, 2 and 3 are 2530, 10 120 and 29 707, respectively.

Figure 2 shows radial profiles of mean axial velocity, $\tilde{U}$, turbulent kinetic energy, k, mean mixture fraction, $\tilde{\xi}$, and its rms fluctuations, ξ', mean temperature, $\tilde{T}$, and its rms fluctuations,
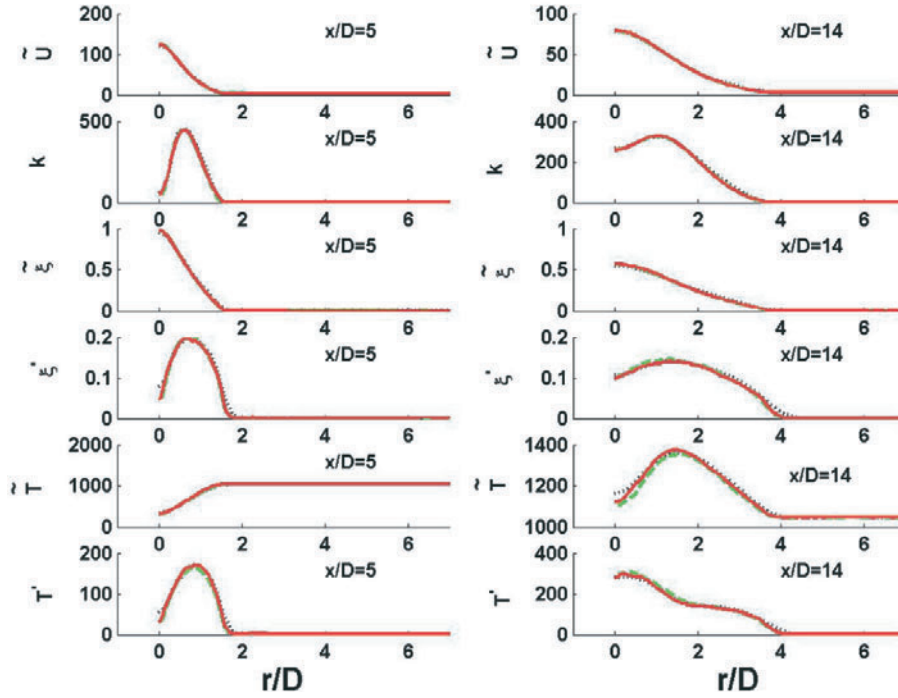
Figure 2. Radial profiles of mean velocity, turbulent kinetic energy, k, mean mixture fraction, $\tilde{\xi}$, its rms fluctuations, ξ', mean temperature, $\tilde{T}$, and its rms fluctuations, T', computed for the lifted flame. Each plot shows three profiles for meshes 1, 2 and 3. Plots on the LHS are for $x/D = 5$ and on the RHS are for $x/D = 14$. Further information about meshes 1, 2 and 3 may be found in table 4. Black dot: mesh 1; green dash: mesh 2; red solid; mesh 3.

T', computed at two axial locations, $x/D = 5$ and $x/D = 14$ in the flame using the GRI21-H$_2$ mechanism. Each plot shows three profiles for meshes 1, 2 and 3. Mesh 1 shows only slight departures from meshes 2 and 3, especially for mean temperature and the fluctuating quantities. Meshes 2 and 3 give very close results and either may be used to produce a grid-independent solution. However, the finer mesh (mesh 3) is selected here and is used in all further calculations.

To ensure that statistically stationary solutions are obtained, two mean quantities are monitored on the centreline at the exit plane of the solution domain. For the non-reacting case, velocity and mixture fraction are monitored, while for the reacting case, this is done for temperature and the mass fraction of OH. Time averaging is performed over the last 50 steps to reduce the statistical variability in mean quantities. Figure 3 shows radial profiles of mean axial velocity, $\tilde{U}$, turbulent kinetic energy, mean mixture fraction, $\tilde{\xi}$, its rms fluctuations, ξ', and mean density, $\langle \rho \rangle$, computed at two axial locations, $x/D = 5$ and $x/D = 14$ in the non-reacting jet. Each plot shows four profiles for 5, 10, 20 and 30 particles per cell. It is clear that profiles computed using 5 and 10 particles per cell deviate slightly from other calculations especially for the rms quantities and on the outer edges of the jet. Twenty and 30 particles are adequate and 20 particles per cell are hence used in all subsequent calculations.

4.2. Performance of ISAT

It is important to choose adequate error tolerances for the ISAT table and for integrating the ordinary differential equations (ODEs) of chemical rates. With an ODE absolute error tolerance
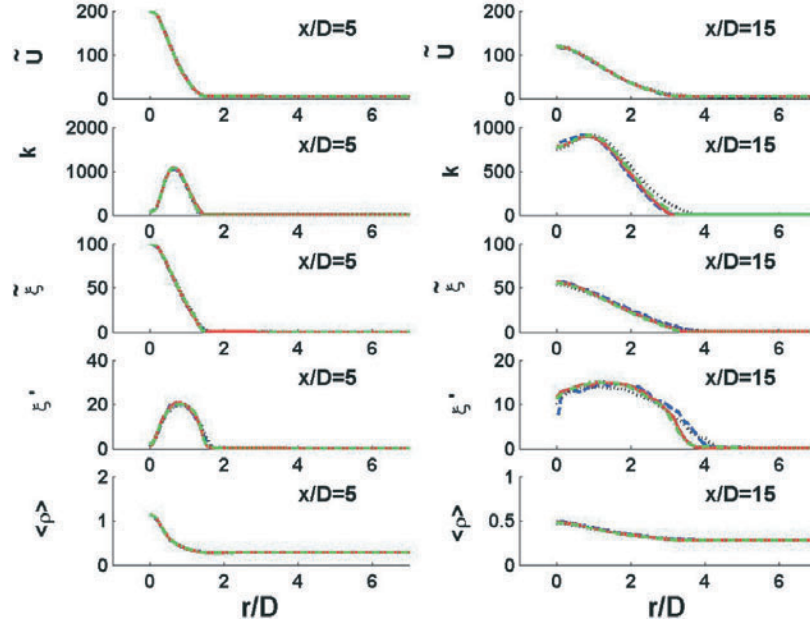
Figure 3. Radial profiles of mean velocity, turbulent kinetic energy, k, mean mixture fraction, $\tilde{\xi}$, its rms fluctuations, ξ', and mean density, $\langle \rho \rangle$, computed using mesh 3 for the non-reacting jet. Each plot shows four profiles computed using 5, 10, 20 and 30 particles per cell. Plots on the LHS are for $x/D = 5$ and on the RHS are for $x/D = 15$. Blue dash: 5; black dot: 10; red solid: 20; green dash dot: 30.

Table 5. Error tolerances used for ISAT and ODE.

	Case 1	Case 2	Case 3	Case 4	Case 5	Case 6
ISAT, ε_{tol}	4×10^{-4}	1×10^{-4}	2.5×10^{-5}	6.25×10^{-6}	1×10^{-6}	6.25×10^{-6}
ODE, ε_{tol}	1×10^{-8}	1×10^{-8}	1×10^{-8}	1×10^{-8}	1×10^{-8}	1×10^{-12}

of 1×10^{-8}, the following ISAT error tolerances are used: 4×10^{-4}, 1×10^{-4}, 2.5×10^{-5}, 6.25×10^{-6} and 1.0×10^{-6}. In order to check the effects of the ODE error tolerance, another calculation was performed with an ISAT error of 6.25×10^{-6} and the ODE error tolerance decreased from 1.0×10^{-8} to 1.0×10^{-12}. The six cases investigated are summarized in table 5. The results of these tests are presented in figure 4, which shows radial profiles of the mean mixture fraction, $\tilde{\xi}$, and its rms fluctuations, ξ', mean temperature, $\tilde{T}$, and the mean mass fractions of OH, $\tilde{Y}_{OH}$, O, $\tilde{Y}_O$, and H, $\tilde{Y}_H$, computed at two axial locations, $x/D = 5$ and $x/D = 14$, in the flame. Each plot shows four profiles for cases 1, 2, 4 and 5 (listed in table 5), all of which are computed using the GRI21-H$_2$ mechanism.

While the mean mixture fraction and its rms fluctuations are only slightly affected, it is clear that decreasing the ISAT error tolerance from 4×10^{-4} to 1×10^{-6} has a significant impact on the calculated temperature and compositional structure of the flame. While an ISAT error tolerance $\varepsilon_{tol} = 4 \times 10^{-4}$ is clearly unacceptable for these calculations, $\varepsilon_{tol} = 6.25 \times 10^{-6}$ is very close to an accurate solution. This change in ε_{tol} has a direct impact on the lift-off height as is clear form figure 5, which shows the conditional mean temperature at the stoichiometric mixture fraction, $\langle T | \xi_s \rangle$, calculated for the range of conditions detailed in table 5. At a given axial location, the conditional mean temperature, $\langle T | \xi_s \rangle$, is calculated as the ensemble average temperature of all particles whose mixture fraction, ξ, is in the range $0.45 < \xi < 0.5$.
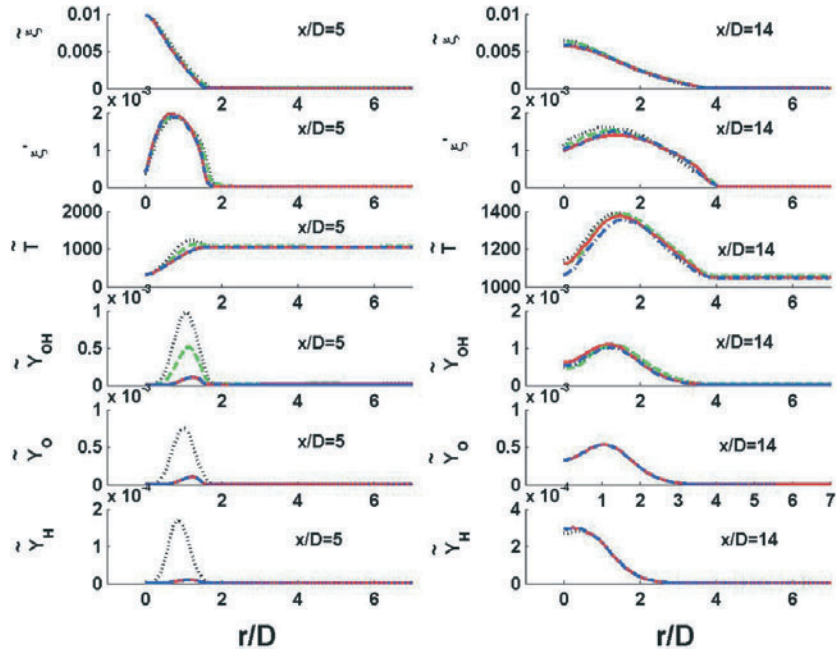
Figure 4. Radial profiles of mean mixture fraction, $\tilde{\xi}$, its rms fluctuations, ξ', mean temperature, $\tilde{T}$, and the mean mass fractions, $\tilde{Y}_{OH}$, $\tilde{Y}_{O}$ and $\tilde{Y}_{H}$, computed for the lifted flame. Each plot shows four profiles computed using an ISAT error tolerance of 4.0×10^{-4}, 1.0×10^{-4}, 6.25×10^{-6} and 1.0×10^{-6}. All calculations use an ODE tolerance of 1.0×10^{-8}. Plots on the LHS are for $x/D = 5$ and on the RHS are for $x/D = 14$. Black dot: 4.0×10^{-4}; green dash: 1.0×10^{-4}; red solid: 6.25×10^{-6}; blue dash dot: 1.0×10^{-6}.

Figure 5 also shows the variation in $\langle T | \xi \rangle$ with respect to ε_{tol} in the region of lift-off at $x/D = 4$–10. It is clear that a numerically accurate solution is only obtained with an ISAT error tolerance $\varepsilon_{tol} = 6.25 \times 10^{-6}$ or lower. Although not shown in figure 5, it is noted that changing the ODE error tolerance from 1×10^{-8} to 1×10^{-12} has little or no impact on the results. A series of tests conducted using the Mueller-H_2 mechanism yields similar conclusions, namely that for a numerically accurate solution to be obtained, the ISAT and ODE error tolerances should be no greater than 6.25×10^{-6} and 1×10^{-8}, respectively. These values are therefore used in all the calculations reported below.

4.3. Computational performance

Calculations are performed on DELL OptiPlex GX400 workstations, which have 1 Gb of RAM and a speed of 2 GHz. All calculations reported here are serial. The number of steps required to reach statistically stationary solutions depends on a number of parameters. Table 6 gives estimates of the number of steps, N, required to reach a statistically stationary solution and the CPU time per step for a number of non-reacting and reacting calculations. A smaller number of iterations are required when finer ISAT tolerances are used. The CPU per time step increases by about 50% as the ISAT tolerances are refined by an order of magnitude. Only approximate numbers are given here since the CPU times vary depending on the starting case and on whether table generation or retrievals are being performed.
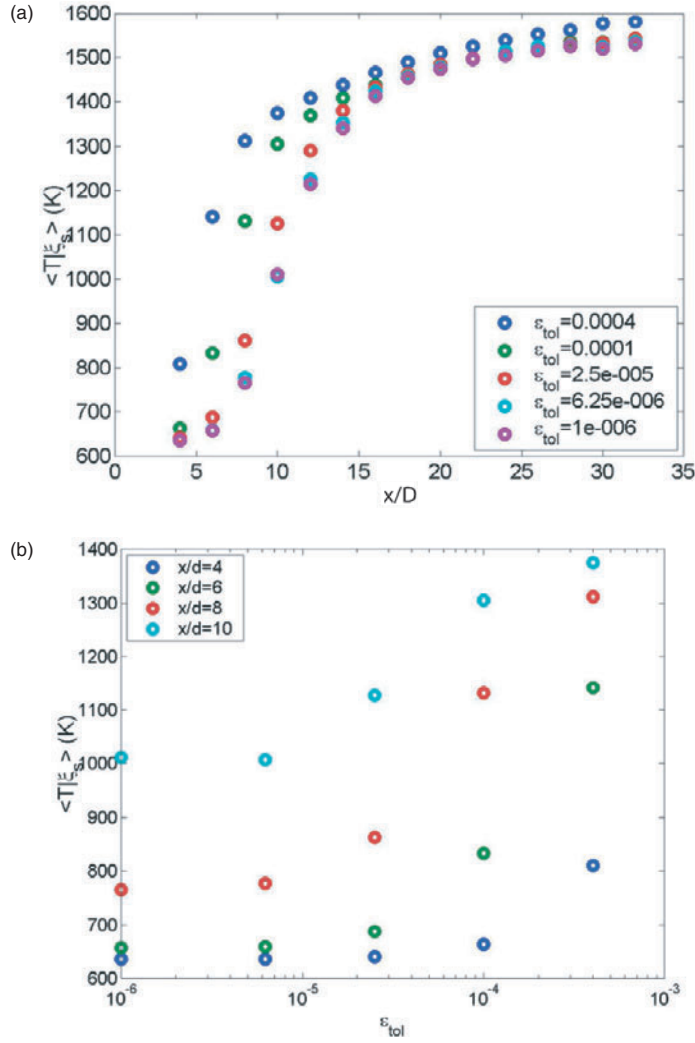
Figure 5. Calculated conditional mean temperature at the stoichiometric mixture fraction, $\langle T|\xi_s \rangle$, in the lifted flame. Plot (*a*) shows the computations versus x/D at ISAT error tolerances of 4.0×10^{-4}, 1.0×10^{-4}, 2.5×10^{-5}, 6.25×10^{-6} and 1.0×10^{-6}. Plot (*b*) shows computations at various x/D plotted against ISAT error tolerance. All calculations use an ODE error tolerance of 1.0×10^{-8}.

Table 6. Computational requirements for a number of selected runs.

	Mechanism	Mesh	Particles per cell	ISAT, ε_{tol}	ODE, ε_{tol}	Number of steps, N	CPU/step (s)
Non-reacting	—	Mesh 1	20	—	—	~1000	~2.5
Non-reacting	—	Mesh 3	20	—	—	~3000	~26
Reacting	GRI21-H$_2$	Mesh 2	20	1.0×10^{-4}	1.0×10^{-8}	~6000	~33
Reacting	GRI21-H$_2$	Mesh 2	20	1.0×10^{-6}	1.0×10^{-8}	~3500	~65
Reacting	Mueller-H$_2$	Mesh 3	20	1.0×10^{-4}	1.0×10^{-8}	~6000	~65
Reacting	Mueller-H$_2$	Mesh 3	20	1.0×10^{-6}	1.0×10^{-8}	—	~180
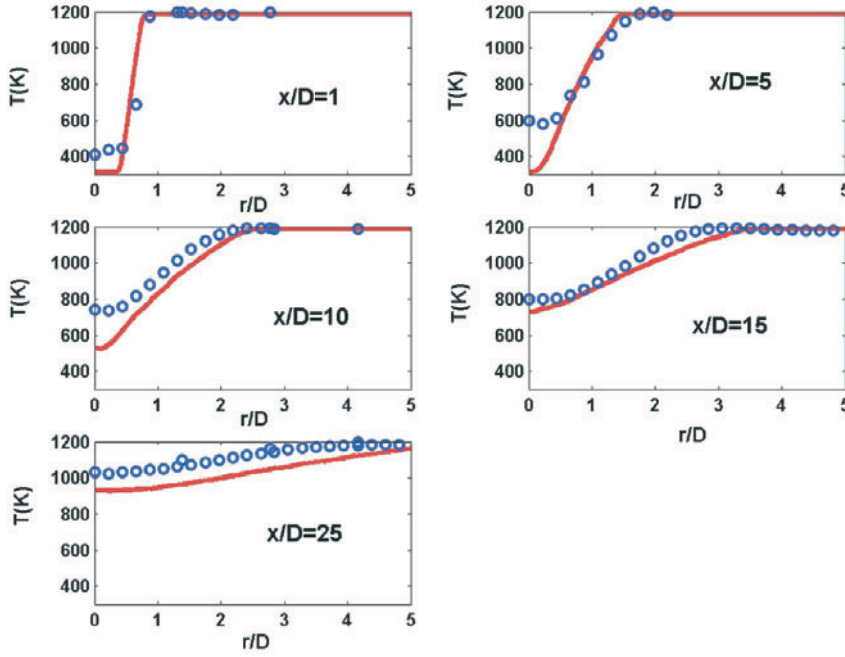
Figure 6. Measured and computed radial profiles of mean temperature, $\tilde{T}$, in the non-reacting jet. Symbols represent measurements. Five plots are shown for $x/D = 1$, 5, 10, 15 and 25. The computations use mesh 3 and 20 particles per cell.

5. Results

The computations presented in this section use the fine mesh (mesh 3) with 20 particles per cell. Mean quantities are obtained by averaging over 50 time steps. For the reacting case, an ISAT error tolerance of 6.25×10^{-6} is used with on ODE error tolerance of 1.0×10^{-8}. Comparisons are made with the data of Cabra and co-workers [30, 31].

5.1. Non-reacting jet

Figure 6 shows radial profiles of the measured and computed temperatures at various axial locations in the non-reacting jet. It should be noted here that the temperature is obtained from the computed density which linearly correlates with mixture fraction. The agreement between measurements and computations is reasonable, given the following qualifications: (i) the k–ε model, with its standard constants, is known to over-predict the spreading rate of cylindrical jets. The standard adjustment of increasing one of the constants, $C_{\varepsilon 1}$, from 1.44 to 1.6, is not effective here, and this is conjectured to be because of the lower density of the co-flow. Differences in density between the jet and the co-flow are known to affect the mixing behaviour of jets [38]. (ii) The disagreement between the measured and computed temperatures on the centreline, particularly near the jet exit plane, is largely due to the fact the heat transfer from the hot co-flow is rather significant and yet not properly accounted for in the computations. Conjugate heat transfer between the jet and the co-flow is the subject of further investigations and this aspect will be enhanced in the next generation of calculations.
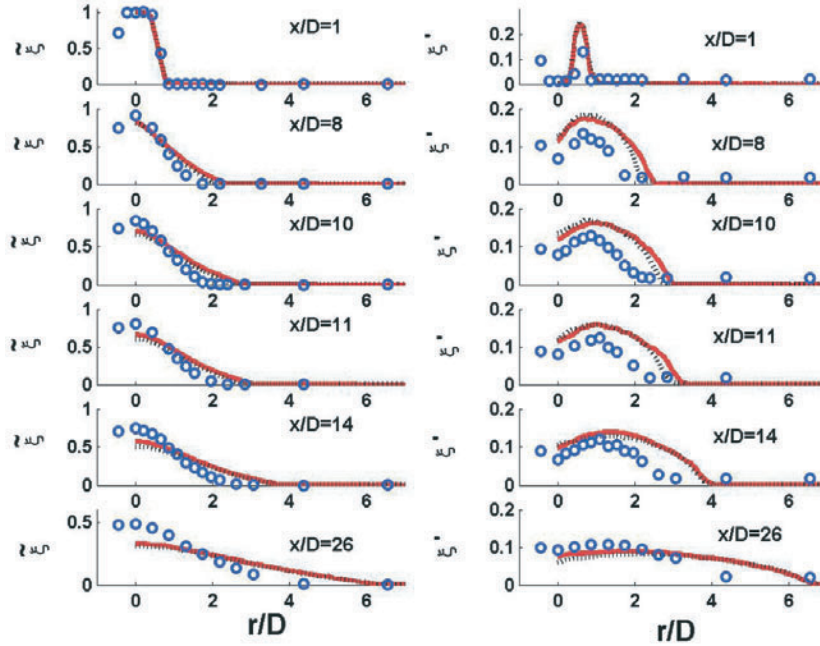
Figure 7. Measured and computed radial profiles of mean mixture fraction, $\tilde{\xi}$, and its rms fluctuations, ξ', for the lifted flame. Plots on the LHS are for $\tilde{\xi}$ and plots on the RHS are for ξ'. Each column shows six plots for axial locations $x/D = 1, 8, 10, 11, 14$ and 26. The symbols in each plot represent measurements, the solid line is computed using the GRI21-H$_2$ mechanism and the dotted line represents computations from the Mueller-H$_2$ mechanism.

5.2. Lifted flame

Figures 7–10 show a comparison between measurements and computations at various axial locations ($x/D = 1, 8, 10, 11, 14, 26$) in the lifted flame. Two scalars are presented in each figure with: mean mixture fraction, $\tilde{\xi}$, and its rms fluctuations, ξ', in figure 7; mean temperature, $\tilde{T}$, and its rms fluctuations, T', presented in figure 8; the mean mass fractions of hydrogen, $\tilde{Y}_{H_2}$, and hydroxyl, $\tilde{Y}_{OH}$, in figure 9; and the mean mass fractions of water, $\tilde{Y}_{H_2O}$, and oxygen, $\tilde{Y}_{O_2}$, in figure 10. Results are presented for both the Mueller-H$_2$ and GRI21-H$_2$ mechanisms.

Figure 7 shows that the measured and computed mixing fields are in good agreement at upstream locations but start to deviate at $x/D \geqslant 11$, with the computations under-predicting $\tilde{\xi}$ and over-predicting the spreading rate of the jet. It should be noted here that increasing the constant $C_{\varepsilon 1}$ from 1.44 to 1.6 does not remedy this deficiency as is normally the case for turbulent jets. This is probably because the jet is issuing in heated air where the density is less than that of the jet fluid. The rms fluctuations of mixture fraction, ξ', are generally over-predicted right across the jet length. This may be overcome by increasing the mixing-model constant, $C\phi$, and this aspect is discussed later. These results are consistent for both the Mueller-H$_2$ and GRI21-H$_2$ mechanisms.

The mean temperature profiles (shown in figure 8) indicate that the lift-off heights computed using the Mueller-H$_2$ and GRI21-H$_2$ mechanisms are very different and bracket the experimental lift-off height, which occurs at about 11 jet diameters as seen from the measured rise in peak temperature. The computed lift-off heights for the GRI21-H$_2$ and Mueller-H$_2$
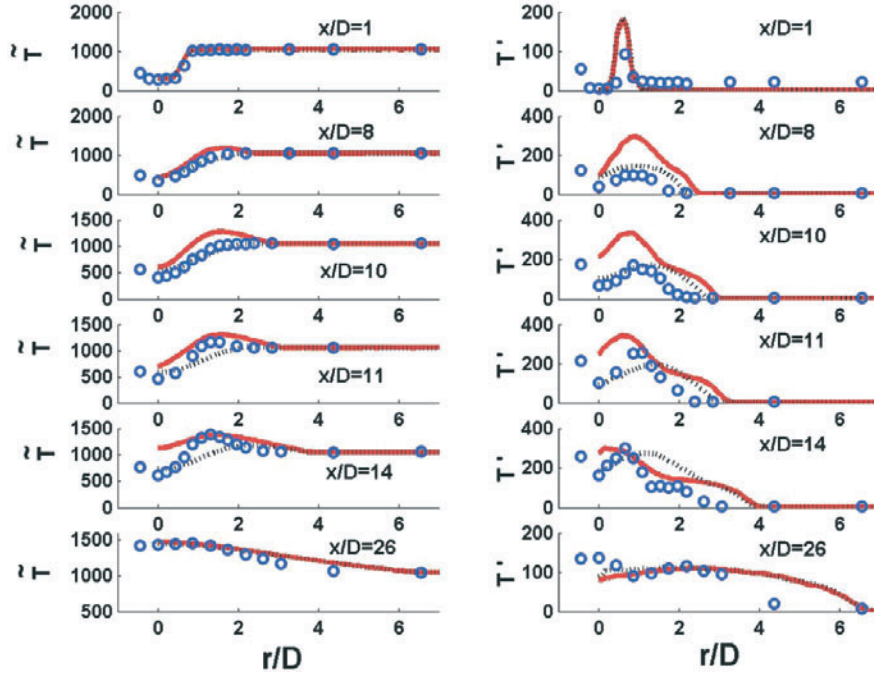
Figure 8. Measured and computed radial profiles of mean temperature, $\tilde{T}$, and its rms fluctuations, T', for the lifted flame. Plots on the LHS are for $\tilde{T}$ and plots on the RHS are for T'. Each column shows six plots for axial locations $x/D = 1$, 8, 10, 11, 14 and 26. The symbols in each plot represent measurements, the solid line is computed using the GRI21-H_2 mechanism and the dotted line represents computations from the Mueller-H_2 mechanism.

mechanisms are $x/D \sim 8$ and 14, respectively. The GRI21-H_2 mechanism results in higher rms fluctuations of temperature, especially at upstream locations. However, the computed profiles of T' using the Mueller-H_2 mechanism are very close to the measurements.

The mean species mass fractions (shown in figures 9 and 10) confirm the results shown earlier for temperature, namely, that the computations using the Mueller-H_2 and GRI21-H_2 mechanisms, generally bracket the experimental results at least for the upstream measurement locations. This is true for the mass fractions of H_2, H_2O, O_2 and OH shown in figures 9 and 10. Further downstream at $x/D = 26$, the peak mass fraction of OH is under-predicted by both mechanisms while the computed profiles of H_2, H_2O and O_2 are adequate except for a discrepancy in the spreading rate that is mainly due to the turbulence model.

Axial profiles of the computed mean temperature and mean mass fractions of OH, O and H are plotted in figure 11 for both Mueller-H_2 and GRI21-H_2 mechanisms and for radial locations $r/D = 0$, 0.5, 1.0 and 1.5, which span the base of the flame. The measured mean centreline temperatures and mass fractions of OH are also shown on the relevant plots. A sharper rise in temperature is observed with the GRI21-H_2 mechanism, and lift-off is first observed at a radial location of about $r/D = 1$. This is also observed in the axial profiles for $\tilde{Y}_{OH}$, $\tilde{Y}_O$ and $\tilde{Y}_H$, which show an increase starting to occur at $r/D = 1.0$ as early as $x/D = 5$. The peak mean mass fraction of oxygen, $\tilde{Y}_O$, occurs first at $x/D = 8$ and this may be taken as the computed location of the flame base. With the Mueller-H_2 mechanism, the profiles of temperature and species mass fractions overlap regardless of the radial locations, implying that lift-off occurs closer to the jet centreline. Gauging by the peak location of species mass fractions, lift-off occurs at about $x/D = 18$, which is further from measurements.
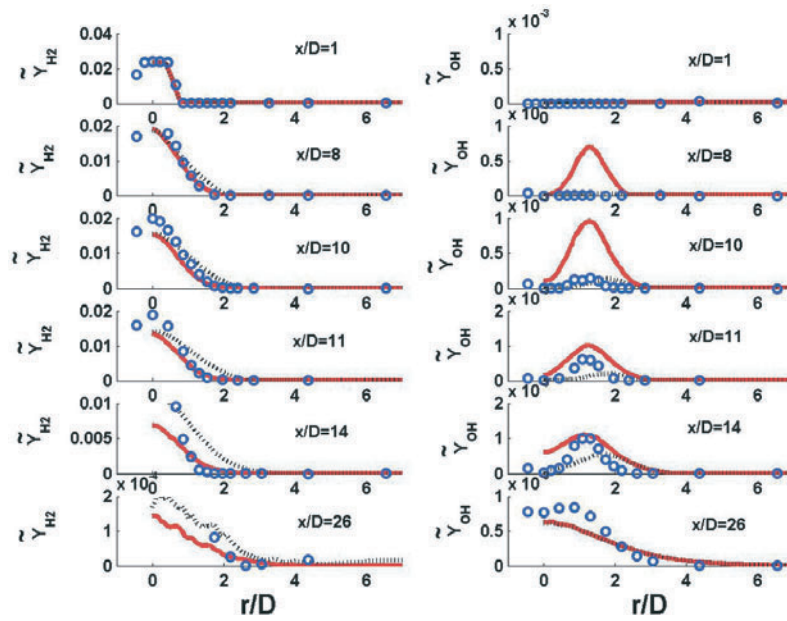
Figure 9. Measured and computed radial profiles of mean mass fractions of H$_2$ and OH, $\tilde{Y}_{H_2}$ and $\tilde{Y}_{OH}$, for the lifted flame. Plots on the LHS are for $\tilde{Y}_{H_2}$ and plots on the RHS are for $\tilde{Y}_{OH}$. Each column shows six plots for axial locations $x/D = 1, 8, 10, 11, 14$ and 26. The symbols in each plot represent measurements, the solid line is computed using the GRI21-H$_2$ mechanism and the dotted line represents computations from the Mueller-H$_2$ mechanism.
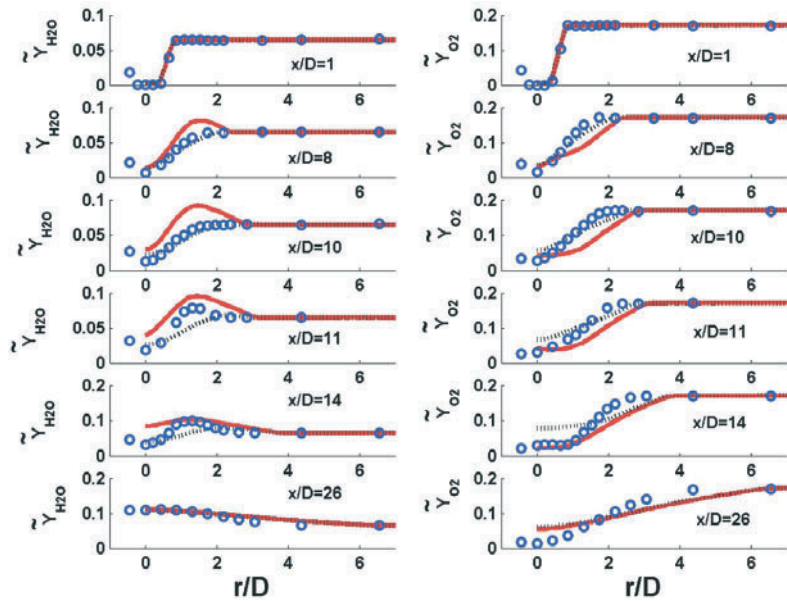
Figure 10. Measured and computed radial profiles of mean mass fractions of H$_2$O and O$_2$, $\tilde{Y}_{H_2O}$ and $\tilde{Y}_{O_2}$, for the lifted flame. Plots on the LHS are for $\tilde{Y}_{H_2O}$ and plots on the RHS are for $\tilde{Y}_{O_2}$. Each column shows six plots for axial locations $x/D = 1, 8, 10, 11, 14$ and 26. The symbols in each plot represent measurements, the solid line is computed using the GRI21-H$_2$ mechanism and the dotted line represents computations from the Mueller-H$_2$ mechanism.
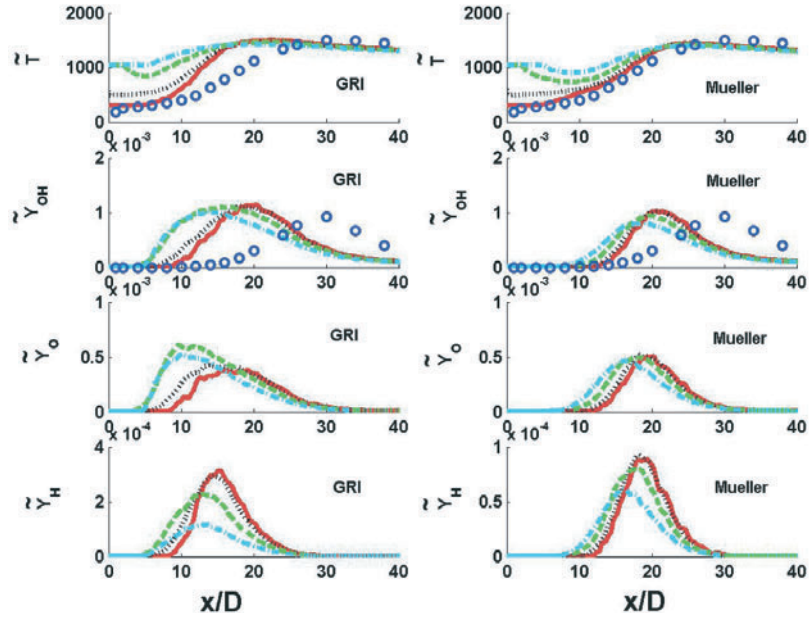
Figure 11. Axial profiles of mean temperature, $\tilde{T}$, and the mean mass fractions $\tilde{Y}_{OH}$, $\tilde{Y}_O$ and $\tilde{Y}_H$ computed for the lifted flame. Plots on the LHS are computed using GRI21-H$_2$ mechanism and plots on the RHS are computed using the Mueller-H$_2$ mechanism. Each plots shows four profiles for $r/D = 0$, 0.5, 1.0 and 1.5. Symbols are measurements for $r/D = 0$. Red solid: $r/D = 0.0$; black dot: $r/D = 0.5$; green dash: $r/D = 1.0$; cyan dash dot: $r/D = 1.5$.

Measured and computed scatter plots of temperature and the mass fraction of OH are shown in figure 12 for various axial locations in the flame. All the data points or fluid samples corresponding to the particular axial location are shown. The computations are obtained using the GRI21-H$_2$ mechanism, and these agree qualitatively well with the measurements. At $x/D = 8$, the domain below the fully burnt limit is similarly populated, indicating the existence of fluid samples that are partially burnt and in the process on igniting. This proportion increases at $x/D = 11$, indicating intense auto-ignition that is almost complete at $x/D = 14$, where most of the data points lie closer to the fully burnt limits.

6. Modelling issues

The hybrid approach adopted in this paper involves a turbulence model, a mixing model and a chemistry model. The turbulence model used here is rather simple and not elaborated further in this paper except for re-stating that changing the constant $C_{\varepsilon 1}$ from 1.44 to 1.6 has become a standard approach that will improve the k–ε calculation of the jet spreading rate. However, this improvement did not occur in the current geometry possibly because the co-flowing mixture in which the jet issues is heated and hence the mixing rates in the jet are affected by the significant density ratio between the jet and the co-flow [38]. The discussion that follows is only concerned with modelling of mixing and chemical reactions.

6.1. Effects of C_ϕ

The MC mixing model used here is also rather simple. Other mixing models that may be used in the future are the IEM and the Euclidean minimum spanning tree (EMST) models [39]. More
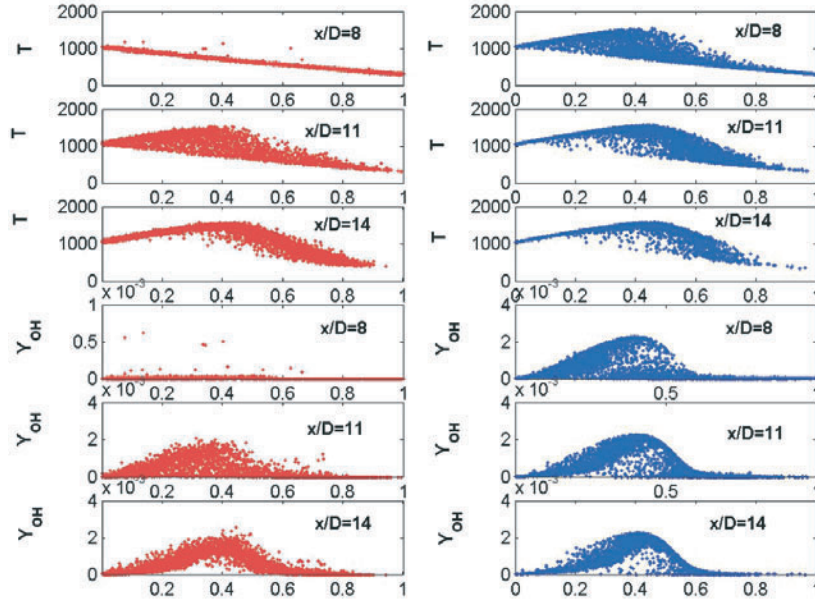
Figure 12. Measured (LHS) and computed (RHS) scatter plots for temperature and the mass fraction of OH, Y$_{OH}$, against mixture fraction, ξ, plotted for $x/D = 8$, 11 and 14. The computations are for the GRI21-H2 mechanism.

sophisticated mixing models are currently being developed by Klimenko and Pope [40]. The constant C_ϕ used with the MC model is changed from $C_\phi = 2.0$, which is the standard value, to $C_\phi = 2.3$ (assumed by Lindstedt and Louloudi [16]) and 20, respectively. Figure 13 shows radial profiles of mean mixture fraction, $\tilde{\xi}$, and its rms fluctuations, ξ', mean temperature, $\tilde{T}$, and its rms fluctuations, T', and the mean mass fractions of OH, $\tilde{Y}_{OH}$, and O, $\tilde{Y}_O$, computed at two axial locations, $x/D = 5$ and $x/D = 14$, in the flame. Each plot shows three profiles computed for $C_\phi = 2.0$, 2.3 and 20. The following points are worth noting.

- Increasing C_ϕ from 2.0 to 2.3 has little impact on the mixing: the rms fluctuations of mixture remain over-predicted as shown earlier. It is worth mentioning here that $C_\phi = 2.3$ was found to be the optimal value in the calculations of Lindstedt and Louloudi [16].
- As expected, increasing C_ϕ from 2.0 to 20 reduces the rms fluctuations significantly and enhances mixing as shown from the profiles of ξ' and T'. Although the flame lift-off height decreases slightly from about eight to six diameters, the flame remains lifted indicating that the lift-off height is affected by the rates of both mixing and chemical reactions. This dependence on the chemical kinetics confirms the auto-ignition characteristics of this jet flame.

6.2. Effects of reaction rates

In order to understand the impact of the reaction rates on auto-ignition, a simple sensitivity analysis has been conducted of both mechanisms using an idealized model problem. A simple one-dimensional channel is set-up (essentially a plug-flow reactor) with a lean but reactive mixture issuing from one end at a velocity of $100 \, \text{m s}^{-1}$. The fluid entering the channel has the following composition: mixture fraction $\xi = 0.05$, temperature $= 1003.03 \, \text{K}$ and mass fractions $Y_{H_2} = 0.001\,171\,29$, $Y_{O_2} = 0.162\,326$, $Y_{H_2O} = 0.061\,319\,1$. This mixture lies along the mixing line formed by the jet and pilot fluid in the flame considered in this paper.
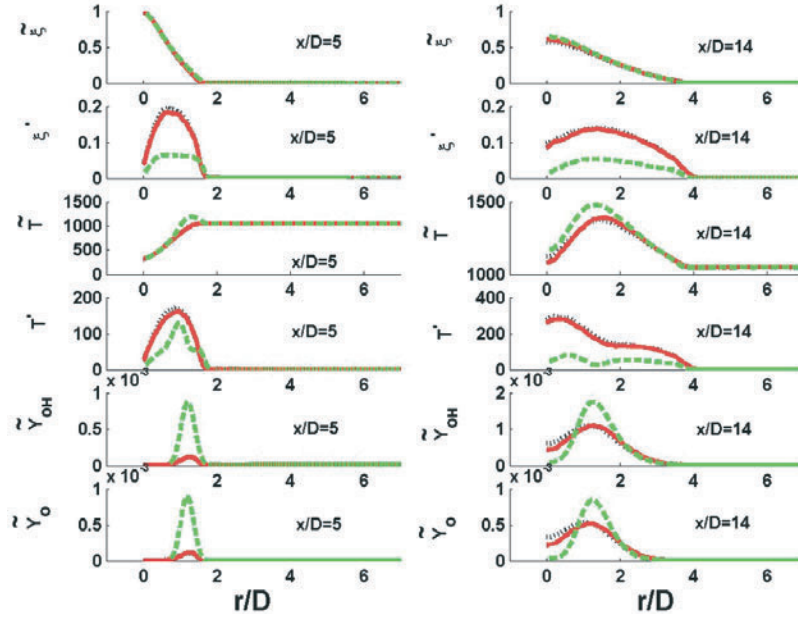
Figure 13. Radial profiles of mean mixture fraction, $\tilde{\xi}$, its rms fluctuations, ξ', mean temperature, $\tilde{T}$, its rms fluctuations, T', and the mean mass fraction of OH and O, $\tilde{Y}_{OH}$ and $\tilde{Y}_O$, computed for the lifted flame. Each plot shows three profiles for $C_\phi = 2.0$, 2.3 and 20. Plots on the LHS are for $x/D = 5$ and on the RHS are for $x/D = 14$. Red solid: $C_\phi = 2.0$; black dot: $C_\phi = 2.3$; green dash: $C_\phi = 20$.

Using the GRI21-H$_2$ mechanism, the mixture auto-ignites at some $x = 125$ mm within the channel, giving a peak temperature of 1118.1 K. Consistent with the turbulent flame results, auto-ignition for the Mueller-H$_2$ mechanism occurs later at $x = 200$ mm. In order to test the impact of individual reactions on auto-ignition, the rate of each reaction is changed separately (by doubling the pre-exponential factor, A) and the computations repeated for the same condition. It is found that some reactions speed-up the auto-ignition process while others cause a delay. The three most dominant reactions that cause a delay or speed-up in auto-ignition are listed for both mechanisms in table 7.

Computations of the lifted flames are now repeated with a modified mechanism where the rate of the reaction that dominates the speed-up of auto-ignition: $O_2 + H \leftrightarrow O + OH$ is doubled. This is reaction 11 in the GRI21-H$_2$ mechanism and reaction 1 in the Mueller-H$_2$ mechanism. The results are summarized in figures 14 and 15, which show the change in composition and lift-off height due to the rate increase.

Figure 14 shows plots of mean temperature, $\tilde{T}$, and mean mass fractions of OH, O and H at various axial locations in the flame computed using the standard and modified GRI21-H$_2$ mechanisms. Figure 15 shows similar plots computed using the standard and modified Mueller-H$_2$ mechanisms. The following points are worth noting.

- As expected, and consistent with the simple channel calculations, auto-ignition occurs earlier and the flame base shifts upstream. Using the computed peak mean mass fraction of oxygen radical as an indicator, the lift-off height of the turbulent flame shifts from $x/D = 8$ to $x/D = 5$ for the GRI21-H$_2$ mechanism and from $x/D = 18$ to $x/D = 9$ for the Mueller-H$_2$ mechanism.
- The peak species mass fractions also change significantly.

Table 7. Reactions from GRI21-H$_2$ and Mueller-H$_2$ mechanisms to which auto-ignition is most sensitive.

	GRI21-H$_2$		Mueller-H$_2$
Reaction number	Reaction	Reaction number	Reaction
	Increasing rate delays auto-ignition		
8	H + O$_2$ + H$_2$O $\leftrightarrow$ HO$_2$ + H$_2$O	13	HO$_2$ + OH $\leftrightarrow$ H$_2$O + O$_2$
9	H + O$_2$ + N$_2$ $\leftrightarrow$ HO$_2$ + N$_2$	12	HO$_2$ + O $\leftrightarrow$ O$_2$ + OH
7	H + O$_2$ + O$_2$ $\leftrightarrow$ HO$_2$ + O$_2$	10	HO$_2$ + H $\leftrightarrow$ H$_2$ + O$_2$
	Increasing rate speeds up auto-ignition		
11	O$_2$ + H $\leftrightarrow$ O + OH	1	O$_2$ + H $\leftrightarrow$ O + OH
3	O + H$_2$ $\leftrightarrow$ H + OH	2	O + H$_2$ $\leftrightarrow$ H + OH
21	H$_2$ + OH $\leftrightarrow$ H$_2$O + H	3	H$_2$ + OH $\leftrightarrow$ H$_2$O + H
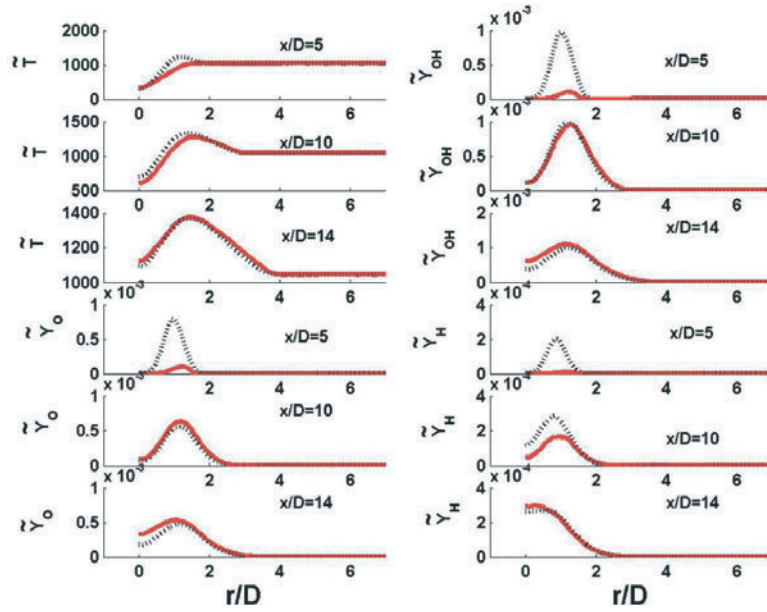
Figure 14. Radial profiles of mean temperature, $\tilde{T}$, and the mean mass fractions $\tilde{Y}_{OH}$, $\tilde{Y}_O$ and $\tilde{Y}_H$ computed using the GRI21-H$_2$ mechanism at three axial locations in the lifted flame, $x/D = 5$, 10 and 14. Each plot shows two profiles, one for the standard mechanism and the other obtained when the rate of reaction 11 is doubled by doubling the pre-exponential factor A. Red solid: standard; black dot: doubled.

- These calculations confirm that the chemical kinetics is very important in controlling the early regions of the turbulent flames studied here. The lift-off height is affected by rates of both mixing and chemical reactions, with there being a marked sensitivity to the rates of the controlling reactions.

7. Discussion

It is clear from the figures presented earlier, especially figure 13, that this flame, although still affected by mixing, is largely controlled by chemical processes. The dependence on the chemical kinetic mechanism is clear, and further investigations are needed to confirm as to which mechanism (and kinetic rates) would be more relevant for the modelling of hydrogen
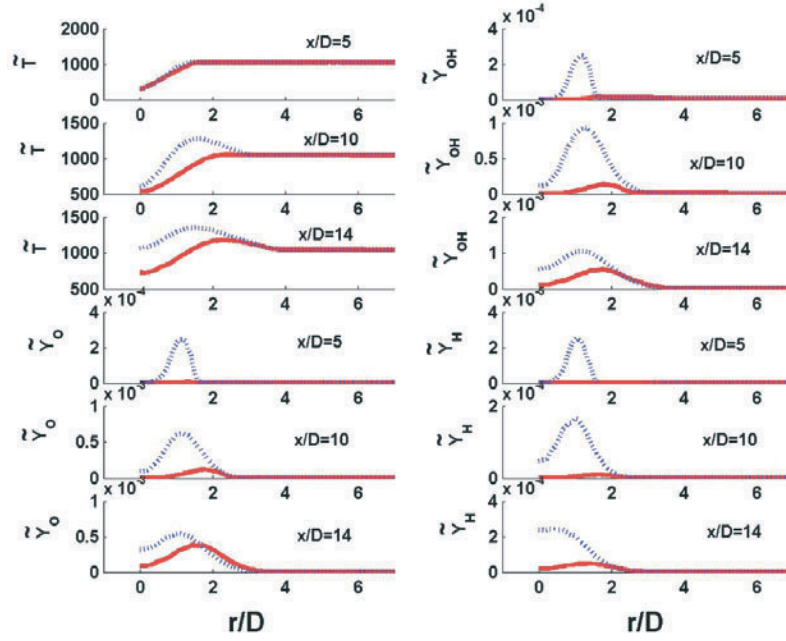
Figure 15. Radial profiles of mean temperature, $\tilde{T}$, and the mean mass fractions $\tilde{Y}_{\mathrm{OH}}$, $\tilde{Y}_{\mathrm{O}}$ and $\tilde{Y}_{\mathrm{H}}$ computed using the Mueller-H_2 mechanism at three axial locations in the lifted flame, $x/D = 5, 10$ and 14. Each plot shows two profiles, one for the standard mechanism and the other obtained when the rate of reaction 1 is doubled by doubling the pre-exponential factor A. Red solid: standard; black dot: doubled.

auto-ignition. What is clear from the calculations presented here is that the GRI21-H_2 and Mueller-H_2 mechanisms straddle the data and the rates of some individual reactions have a huge impact on the lift-off height as well as the flame composition.

A conclusive statement as to the presence of auto-ignition or flame propagation processes at the flame base cannot be made here. Experimentally, the flame is very sensitive to the temperature in the co-flowing pilot and changes, at least qualitatively, from a quietly lifted flame to a noisy flame with larger fluctuations at the base as the pilot temperature decreases. It is not clear whether this implies a definite transition from auto-ignition to premixed flame propagation, or simply a co-existence of both processes. This issue is clearly of importance and warrants further investigation.

Proceeding with the view that auto-ignition does indeed take place, an important question to address here is which mixture fraction range is most responsible for auto-ignition. This is an interesting issue that is explored a little further in this section. The excess temperature, T_{excess}, conditional on mixture fraction is plotted versus axial location is figure 16 for calculations using both the GRI21-H_2 and Mueller-H_2 mechanisms. The excess temperature is representative of the heat release and is defined as $T_{\mathrm{excess}} = T - T_{\mathrm{mixing}}$, where T is the computed temperature and T_{mixing} is the mixing temperature at the mixture fraction of the fluid sample. Three mixture fraction bands are shown in the three plots presented here: $0 < \xi < 0.1$, $0.1 < \xi < 0.2$ and $0.2 < \xi < 0.3$. It is seen that fluid samples in the mixture fraction range $0 < \xi < 0.1$ ignite at earlier axial locations than richer mixtures. This is expected since hot co-flowing gases from the pilot will first mix with enough jet fuel to produce lean mixtures that are hot and hence have short ignition delays. Richer mixtures will have lower temperatures and hence longer ignition delays.
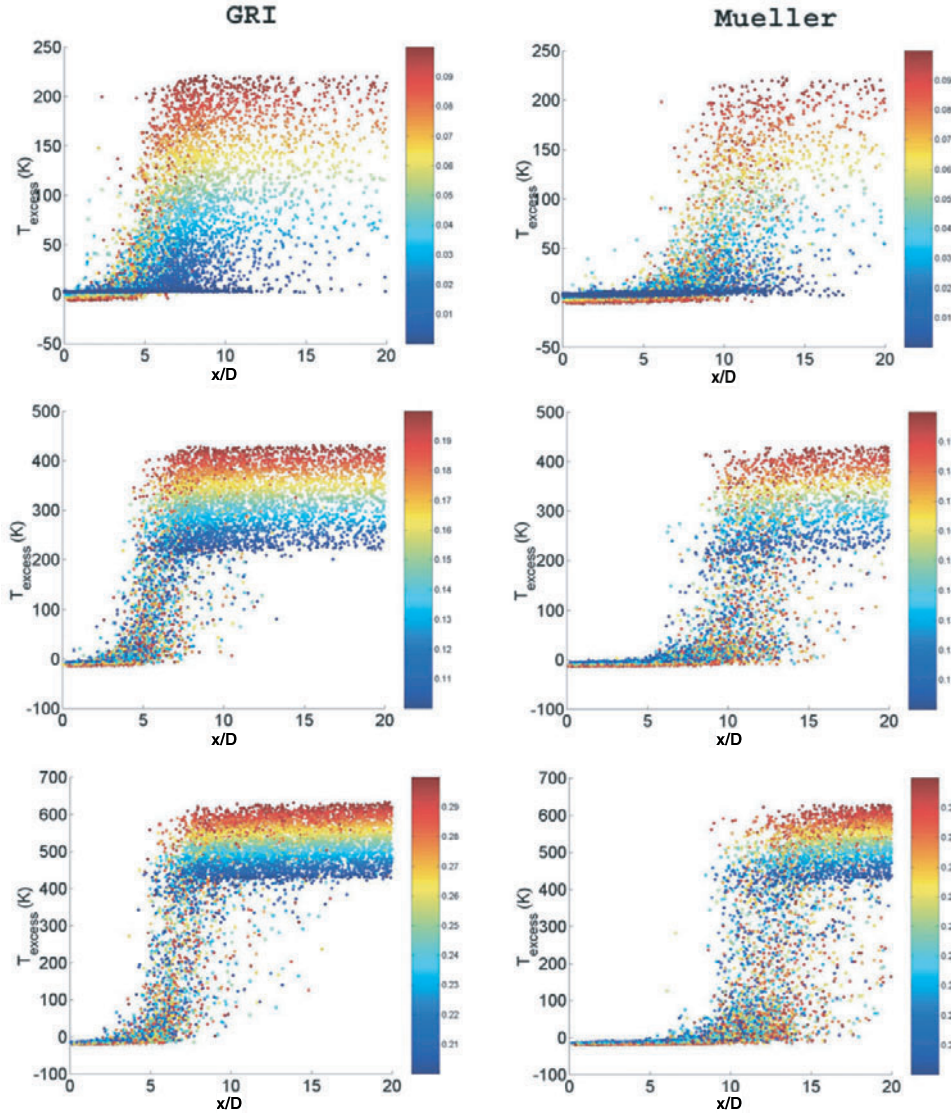
Figure 16. Scatter plots of the excess temperature, $T_{\text{excess}} = T - T_{\text{mixing}}$, conditional with respect to mixture fraction and plotted versus axial location. Three plots are presented for three mixture fraction bands with ranges (from top to bottom) $0 < \xi < 0.1$, $0.1 < \xi < 0.2$ and $0.2 < \xi < 0.3$.

This finding is consistent with separate calculations made using the simple channel flow problem discussed earlier. It is also consistent with the reported findings from DNS studies [24–28]. Fluid samples in the mixture fraction range $0 < \xi < 0.1$ have the fastest ignition rate and this is controlled purely by chemical kinetics rather than mixing. These conclusions apply for both the GRI21-H$_2$ and Mueller-H$_2$ mechanisms.

8. Conclusions

The hybrid RANS–PDF (composition) approach is used here to compute successfully the structure of lifted flames issuing in a vitiated co-flow. Two chemical kinetic mechanisms are

implemented using the ISAT approach. Numerically accurate solutions are obtained after a significant testing for grid convergence, number of particles per cell and error tolerances associated with the ISAT approach.

It is found that, although mixing rates are still important, the flame is largely controlled by the chemical kinetics and the mechanisms used give lift-off heights that straddle the experimental data. The computed mean temperatures and species mass fractions also compare favourably with experimental data. At downstream locations, the flow and mixing fields deviate further from experiments in line with what is expected for the k–ε model.

The lift-off height and flame composition at the stabilization base are extremely sensitive to the rates of some individual reactions, hence stressing the importance of chemical kinetics in this flow configuration. For the fuel mixture used here, it is found that the shortest ignition delays are obtained for lean mixtures spanning the mixture fraction range $0.0 < \xi < 0.1$.

Acknowledgments

Appendix

Table A1. The GRI21-H$_2$ mechanism, with $k = AT^{**b} \exp(-E/RT)$, where A is the pre-exponent factor in mole cm s K and E is the activation energy is cal mole^{-1}.

Reaction number		A	b	E
1	$O + O + M \leftrightarrow O_2 + M$	1.20E+17	−1.0	0.0
	H$_2$/2.4/ H$_2$O/15.4/ Ar/0.83/			
2	$O + H + M \leftrightarrow OH + M$	5.00E+17	−1.0	0.0
	H$_2$/2.0/ H$_2$O/6.0/ Ar/0.7/			
3	$O + H_2 \leftrightarrow H + OH$	5.00E+04	2.67	6 290.0
4	$O + HO_2 \leftrightarrow OH + O_2$	2.00E+13	0.0	0.0
5	$O + H_2O_2 \leftrightarrow OH + HO_2$	9.63E+06	2.0	4 000.0
6	$H + O_2 + M \leftrightarrow HO_2 + M$	2.80E+18	−0.86	0.0
	O$_2$/0.0/ H$_2$O/0.0/ N$_2$/0.0/ Ar/0.0/			
7	$H + O_2 + O_2 \leftrightarrow HO_2 + O_2$	3.00E+20	−1.72	0.0
8	$H + O_2 + H_2O \leftrightarrow HO_2 + H_2O$	9.38E+18	−0.76	0.0
9	$H + O_2 + N_2 \leftrightarrow HO_2 + N_2$	3.75E+20	−1.72	0.0
10	$H + O_2 + Ar \leftrightarrow HO_2 + Ar$	7.00E+17	−0.8	0.0
11	$H + O_2 \leftrightarrow O + OH$	8.30E+13	0.0	14 413.0
12	$H + H + M \leftrightarrow H_2 + M$	1.00E+18	−1.0	0.0
	H$_2$/0.0/ H$_2$O/0.0/ Ar/0.63/			
13	$H + H + H_2 \leftrightarrow H_2 + H_2$	9.00E+16	−0.6	0.0
14	$H + H + H_2O \leftrightarrow H_2 + H_2O$	6.00E+19	−1.25	0.0
15	$H + OH + M \leftrightarrow H_2O + M$	2.20E+22	−2.0	0.0
	H$_2$/0.73/ H$_2$O/3.65/ Ar/0.38/			
16	$H + HO_2 \leftrightarrow O + H_2O$	3.97E+12	0.0	671.0
17	$H + HO_2 \leftrightarrow H_2 + O_2$	2.80E+13	0.0	1 068.0
18	$H + HO_2 \leftrightarrow OH + OH$	1.34E+14	0.0	635.0
19	$H + H_2O_2 \leftrightarrow HO_2 + H_2$	1.21E+07	2.0	5 200.0
20	$H + H_2O_2 \leftrightarrow OH + H_2O$	1.00E+13	0.0	3 600.0
21	$OH + H_2 \leftrightarrow H + H_2O$	2.16E+08	1.51	3 430.0

Table A1. (Continued.)

Reaction Number		A	b	E
22	OH + OH(+M) $\leftrightarrow$ H$_2$O$_2$(+M)	7.40E+13	-0.37	0.0
	LOW/2.3E+18 -0.9 -1.7E+3			
	TROE/0.7346 94.0 1756.0 5182.0/			
	H$_2$/2.0/ H$_2$O/6.0/ Ar/0.7/			
23	OH + OH $\leftrightarrow$ O + H$_2$O	3.57E+04	2.4	$-2\,110.0$
24	OH + HO$_2$ $\leftrightarrow$ H$_2$O + O$_2$	2.90E+13	0.0	-500.0
25	H + H$_2$O$_2$ $\leftrightarrow$ HO$_2$ + H$_2$O	1.75E+12	0.0	320.0
26	H + H$_2$O$_2$ $\leftrightarrow$ HO$_2$ + H$_2$O	5.80E+14	0.0	9\,560.0
27	HO$_2$ + HO$_2$ $\leftrightarrow$ O$_2$ + H$_2$O$_2$	1.30E+11	0.0	$-1\,630.0$
28	HO$_2$ + HO$_2$ $\leftrightarrow$ O$_2$ + H$_2$O$_2$	4.20E+14	0.0	12\,000.0

Table A2. The Mueller-H$_2$ mechanism, with $k = AT^{**b} \exp(-E/RT)$, where A is the pre-exponent factor in mole cm s K and E is the activation energy is cal mole^{-1}.

Reaction number		A	b	E
1	H + O$_2$ $\leftrightarrow$ O + OH	1.915E+14	0.0	16\,439.0
2	O + H$_2$ $\leftrightarrow$ H + OH	0.508E+05	2.67	6\,290.0
3	H$_2$ + OH $\leftrightarrow$ H$_2$O + H	0.216E+09	1.51	3\,430.0
4	O + H$_2$O $\leftrightarrow$ OH + OH	2.970E+06	2.02	13\,400.0
5	H$_2$ + M $\leftrightarrow$ H + H + M	4.577E+19	-1.40	104\,380.0
	H$_2$/2.5/ H$_2$O/12/			
6	O + O + M $\leftrightarrow$ O$_2$ + M	6.165E+15	-0.50	0.0
	H$_2$/2.5/ H$_2$O/12/			
7	O + H + M $\leftrightarrow$ OH + M	4.714E+18	-1.00	0.0
8	H + OH + M $\leftrightarrow$ H$_2$O + M	2.212E+22	-2.00	0.0
	H$_2$/2.5/ H$_2$O/6.3/			
9	H + O$_2$(+M) $\leftrightarrow$ HO$_2$(+M)	1.475E+12	0.60	0.0
	LOW/3.482E+16 -0.411 -1.115E+3			
	TROE/0.5 1E-30 1E+30/			
	H$_2$/2.5/ H$_2$O/12/			
10	HO$_2$ + H $\leftrightarrow$ H$_2$ + O$_2$	1.66E+13	0.0	823.0
11	HO$_2$ + H $\leftrightarrow$ OH + OH	7.079E+13	0.0	295.0
12	HO$_2$ + O $\leftrightarrow$ O$_2$ + OH	0.325E+14	0.0	0.0
13	HO$_2$ + OH $\leftrightarrow$ H$_2$O + O$_2$	2.890E+13	0.0	-497.0
14	HO$_2$ + HO$_2$ $\leftrightarrow$ H$_2$O$_2$ + O$_2$	4.200E+14	0.0	11\,982.0
15	HO$_2$ + HO$_2$ $\leftrightarrow$ H$_2$O$_2$ + O$_2$	1.300E+11	0.0	$-1\,629.0$
16	H$_2$O$_2$(+M) $\leftrightarrow$ OH + OH(+M)	2.951E+14	0.0	48\,430.0
	LOW/1.202E+170.0 + 4.55E+4			
	TROE/0.5 1E-30 1E+30/			
	H$_2$/2.5/ H$_2$O/12/			
17	H$_2$O$_2$ + H $\leftrightarrow$ H$_2$O + OH	0.241E+14	0.0	3\,970.0
18	H$_2$O$_2$ + H $\leftrightarrow$ HO$_2$ + H$_2$	0.482E+14	0.0	7\,950.0
19	H$_2$O$_2$ + O $\leftrightarrow$ OH + HO$_2$	9.550E+06	2.0	3\,970.0
20	H$_2$O$_2$ + OH $\leftrightarrow$ HO$_2$ + H$_2$O	1.000E+12	0.0	0.0
21	H$_2$O$_2$ + OH $\leftrightarrow$ HO$_2$ + H$_2$O	5.800E+14	0.0	9\,557.0

References

[1] Vanquickenborne L and Van Tiggelen A 1996 *Combust. Flame* **10** 59–69
[2] Broadwell J E, Dahm W J A and Mungal M G 1984 *Proc. Combust. Inst.* **20** 303–10

[3] Pitts W M 1990 *Proc. Combust. Inst.* **23** 661–8

[4] Pitts W M 1988 *Proc. Combust. Inst.* **22** 809–16

[5] Kalghatgi G T 1984 *Combust. Sci. Technol.* **41** 17–29
    Kalghatgi G T 1981 *Combust. Sci. Technol.* **26** 233–9

[6] Eickhoff H, Lenze B and Leuckel W 1984 *Proc. Combust. Inst.* **20** 311–8

[7] Gollahalli S R, Savas Ö, Huang R F and Rodriquez Azara J L 1986 *Proc. Combust. Inst.* **21** 1463–71

[8] Takahashi F and Schmoll W J 1990 *Proc. Combust. Inst.* **23** 677–83

[9] Peters N and Williams F A 1983 *AIAA J.* **21** 423–9

[10] Schefer R W, Namazian M and Kelly J 1990 *Proc. Combust. Inst.* **23** 669–76

[11] Kelman J B and Masri A R 1998 *Combust. Sci. Technol.* **135** 117–34

[12] Tacke M M, Geyer D, Hassel E P and Janicka J 1998 *Proc. Combust. Inst.* **27** 1157–65

[13] Upatnieks A, Driscoll J F and Ceccio S L 2002 *Proc. Combust. Inst.* **29** 1897–903

[14] Tang Q, Xu J and Pope S B 2000 *Proc. Combust. Inst.* **28** 133–40

[15] Lindstedt R P, Louloudi S A and Vaos E M 2000 *Proc. Combust. Inst.* **28** 149–56

[16] Lindstedt R P and Louloudi S A 2002 *Proc. Combust. Inst.* **29** 2147–54

[17] Liu K, Pope S B and Caughey D A 2003 Calculations of a turbulent bluff-body stabilized flame *3rd Joint Meeting of the US Sections of the Combustion Institute (Chicago, March 2003)*

[18] Klimenko A Yu 1990 *Fluid Dyn.* **25** 327–34

[19] Bilger R W 1993 *Phys. Fluids* A **5** 436–44

[20] Kim S H, Huh K Y and Bilger R W 2002 *Proc. Combust. Inst.* **29** 2131–7

[21] Pitsch H 2002 *Proc. Combust. Inst.* **29** 2679–85

[22] Mastorakos E T A, Baritaud B and Poinsot T J 1997 *Combust. Flame* **109** 198–223

[23] Mastorakos E T A, da Cruz T A, Baritaud B and Poinsot T J 1997 *Combust. Sci. Technol.* **125** 243–82

[24] Sreedhara H and Lakshmisha K N 2000 *Proc. Combust. Inst.* **28** 25–34

[25] Sreedhara H and Lakshmisha K N 2002 *Proc. Combust. Inst.* **29** 2051–9

[26] Sreedhara H and Lakshmisha K N 2002 *Proc. Combust. Inst.* **29** 2069–77

[27] Hilbert R and Thevenin D 2002 *Combust. Flame* **128** 22–37

[28] Hilbert R, Tap F, Veynante D and Thevenin D 2002 *Proc. Combust. Inst.* **29** 2079–85

[29] Dally B B, Karpetis A N and Barlow R S 2002 *Proc. Combust. Inst.* **29** 1147–54

[30] Cabra R, Myrvold T, Chen J Y, Dibble R W, Karpetis A N and Barlow R S 2002 *Proc. Combust. Inst.* **29** 1881–8

[31] Cabra R, http://www.me.berkeley.edu/cal/VCB/

[32] Pope S B 1997 *Combust. Theory Modelling* **1** 1–24

[33] Mueller M A, Kim T J, Yetter R A and Dryer F L 1999 Flow reactor studies and kinetic modeling of the H_2/O_2 reaction *Int. J. Chem. Kinetics* **31** 113–25

[34] Bowman C T, Hanson R K, Davidson D F, Gardiner Jr, Lissianski V, Smith G P, Golden D M, Goldenberg M and Frenklach M 1999 Gri-Mech 2.11 http://www.me.berkeley.edu/gri_mech/

[35] Kreutz T G and Law C K 1996 *Combust. Flame* **104** 157–75

[36] Im H G, Chen J H and Law C K 1998 *Proc. Combust. Inst.* **27** 1047–56

[37] Maas U and Warnatz J 1988 *Proc. Combust. Inst.* **22** 1695–704

[38] Pitts W M 1991 *Exp. Fluids* **11** 125–34
     Pitts W M 1991 *Exp. Fluids* **11** 135–41

[39] Subramanian S and Pope S B 1998 *Combust. Flame* **115** 487–514

[40] Klimenko A Yu and Pope S B 2003 *Phys. Fluids* **15** 1907–25